Supporting Information:

Calculating apatite dissolution and stocks

1) **A function to model apatite dissolution.** Apatite dissolution is dependent on temperature, pH, solution saturation state, apatite composition, and apatite surface area (Guidry and Mackenzie 2003). Also, the abundance of organic acids may impact dissolution, leading to much slower apatite dissolution in organic matter-rich soils (Le Roux 2006). While temperature and pH are known for our soils, solution saturation state, apatite composition, and apatite surface area are not, and likely very different in heterogeneous soil environment compared to lab conditions. Given the lack of data on the complex micro-scale processes, rather than fitting a mechanistic model, we thus fit a simple, explorative model based on observations of dust-derived apatite dissolution in a humid chronosequence (Eger et al., 2013) and a peat bog (Le Roux et al., 2006). Assuming first order decay, apatite dissolution can be modeled with Eq. 1.

$$P(t) = P_0 * e^{-k*t} \qquad \text{(Eq. 1)},$$

Where P_0 is the annual apatite input in mg P m^{-2} yr^{-1}, $P(t)$ is the apatite remaining from one input year after t years, and k is the apatite dissolution rate.

2) **Estimating apatite dissolution rate**. In a peat bog in Germany, dust-derived apatite was found to persist to a depth of 8 cm, which 210Pb and 14C based age-depth modeling showed to be 50 – 100 years old (Le Roux 2006). Similarly, by studying dust inputs along a chronosequence, authors estimated that dust-derived apatite grains endure up to 200 years in wet, low pH soils in New Zealand (Eger et al. 2013). The persistence reported by these studies gives us information about the temporal decay of dust-derived apatite in humid, acidic soils; however, these studies did not report detection limits, so it is not clear what fraction of apatite remaining ($P(t)/P_0$) corresponds with these times. However, if we consider all possible combinations of the reported times t and reasonable values for fractions of apatite remaining to fall below detection limit (0.01, 0.1, and 0.2), we can approximate a broad range of potential apatite dissolution rates with Eq. 2.

$$\frac{P(t)}{P_0} = e^{-k*t} \qquad \text{(Eq. 2)},$$

Solving for k,

$$k = -\frac{\ln\left(\frac{P_{(t)}}{P_0}\right)}{t} \text{ (Eq. 3)},$$

For the above mentioned combinations, k ranges from 0.008 to 0.092 yr^{-1}.

time [yr]	$P(t)/P_0$	apatite dissolution rate [yr^{-1}][a]	apatite stocks [mg P m^{-2}][b]	apatite stocks [mg P kg^{-1}][c]
50	0.01	0.092	293	7.3
50	0.1	0.046	587	14.7
50	0.2	0.032	844	21.1
200	0.01	0.023	1174	29.3
200	0.1	0.012	2250	56.3
200	0.2	0.008	3375	84.4

[a]calculated with Eq. 1

[b]calculated with Eq. 2

[c]calculated using bulk density and A horizon depth

3) **Estimating Aeolian apatite stocks.** To calculate the Aeolian apatite stocks, we integrate the Aeolian apatite input over the age of the soil, considering the dissolution rate (Eq. 4).

$$P_{stock} = \int_0^{150000} P_0 * e^{-k*t} * dt \qquad \text{(Eq. 4)},$$

Solving the definite integral yields,

$$P_{stock} = (1 - e^{-150000k}) * \frac{P_0}{k} \qquad \text{(Eq. 5)}$$

Given an annual apatite P input of 27 mg P m^{-2} yr^{-1} and for the range of *k* calculated above, we get a P_{stock} range from 290 – 3400 mg P m^{-2}. Since P pools are usually given in mg kg^{-1} basis, stocks are converted to a mass concentration given the soil horizon depth (10 cm, (Helfenstein et al. 2018)) and the soil bulk density (0.4 g cm^{-3}, (Chadwick et al. 2003)). This gives a per mass pool size of Aeolian apatite of 7.3 – 84 mg P kg^{-1} soil, or 0.2 to 2.3% of total P. Given the uncertainties inherent in the approximation using our simple, exploratory model, we opt to present only orders of magnitude in the main text.

Note: Though dust input changed over time, this source of error should have minimal effect on the calculation of stocks, since recent inputs dominate the stocks (see Eq. 1). To account for uncertainties associated with the approximations, in the text only orders of magnitude are presented.

References

Chadwick O a., Gavenda RT, Kelly EF, et al (2003) The impact of climate on the biogeochemical functioning of volcanic soils. Chem Geol 202:195–223. doi: 10.1016/j.chemgeo.2002.09.001

Eger A, Almond PC, Condron LM (2013) Phosphorus fertilization by active dust deposition in a super-humid, temperate environment - Soil phosphorus fractionation and accession processes. Global Biogeochem Cycles 27:108–118. doi: 10.1002/gbc.20019

Guidry MW, Mackenzie FT (2003) Experimental study of igneous and sedimentary apatite dissolution: Control of pH, distance from equilibrium, and temperature on dissolution rates. Geochim Cosmochim Acta 67:2949–2963. doi: 10.1016/S0016-7037(03)00265-5

Helfenstein J, Tamburini F, von Sperber C, et al (2018) Combining spectroscopic and isotopic techniques gives a dynamic view of phosphorus cycling in soil. Nat Commun 9:3226. doi: 10.1038/s41467-018-05731-2

Jackson ML, Levelt TWM, Syers JK, et al (1971) Geomorphological Relationships of Tropospherically Derived Quartz in the Soils of the Hawaiian Islands1. Soil Sci Soc Am J 35:515–525. doi: 10.2136/sssaj1971.03615995003500040015x

Le Roux G, Laverret E, Shotyk W (2006) Fate of calcite, apatite and feldspars in an ombrotrophic peat bog, Black Forest, Germany. J Geol Soc London 163:641–646. doi: 10.1144/0016-764920-035

Table S1. Extended information on sampling sites. From Helfenstein et al. (2018). MAP = mean annual precipitation; PET = potential evapotranspiration; Lat = Latitude; Long = Longitude.

site	MAP [mm yr^{-1}]	MAP - PET [mm yr^{-1}]	elevation [m]	Lat	Long	sampling depth A horizon	sampling depth B horizon
1	275	-1487	70	20.113	-155.88	0-6	6-18
2	316	-1499	128	20.116	-155.874	0-8	8-20
3	1340	-328	619	20.148	-155.831	0-15	15-40
4	1578	-77	735	20.151	-155.821	0-30	30-50
5	2163	620	860	20.156	-155.797	0-15	25-50
6	3123	1761	1059	20.135	-155.748	0-10	25-50

Table S2: Soil properties of the analyzed Hawaiian soils. MAP = mean annual precipitation.

Site-Horizon		MAP	pH	C	N	P	Si	Al	Fe	Ca
		mm yr^{-1}	*in water*	*g kg^{-1}*	*g kg^{-1}*	*g kg^{-1}*	*g kg^{-1}*	*g kg^{-1}*	*g kg^{-1}*	*g kg^{-1}*
1	A	275	6.7	14	1.3	5.2	108	122	132	7.6
	B	275	7.4	36	2.4	4.1	73	125	130	13.3
2	A	316	6.4	29	2.5	5.9	105	122	127	8.9
	B	316	6.5	38	2.8	4.6	82	127	124	9.3
3	A	1340	6.3	86	8.3	17.7	85	89	76	18.4
	B	1340	6.6	31	3.1	21.0	93	110	90	19.2
4	A	1578	5.9	73	7.0	6.1	93	101	100	5.2
	B	1578	6.5	63	5.9	10.6	76	105	84	9.4
5	A	2163	5.4	178	13.0	5.5	62	48	111	2.0
	B	2163	5	102	4.9	5.0	64	76	137	0.5
6	A	3123	4.2	230	18.0	3.6	78	42	40	1.1
	B	3123	4.6	138	7.7	4.6	67	92	37	0.5

Table S3: XRD results of the soil from Kohala climosequence on Hawaii; SOM = 2x Corg conc (Pribyl 2010). In g kg-1.

site	horizon	SOM	amorphous minerals	olivines	pyroxenes	plagioclases	alkali feldspars	phosphates		oxides				phyllo-silicates			feldspathoids	quartz	goodness of fit	
								apatite	crandallite	hematite	magnetites	ilmenites	anatase	kaolinite/ halloysite	muscovite	illite	nepheline		R_{wp}	c^2
parent material				58	83	425	248	56			41	34		24	14		15		5.18	0.19
1	A	29	586	54	7	39	49	5		18	41	30	7	123				12	5.52	0.19
	B	74	494	62	31	66	18	13		39	39	37	8	103				16	5.39	0.19
2	A	57	511	61	14	51	25	8		19	49	39	8	143				14	5.31	0.21
	B	76	563	55	9	28	28	10		17	41	37	7	114				14	5.56	0.18
3	A	172	530	23		34	35		49	4	13	7	6	78		19		29	5.45	0.16
	B	62	587	23		39	38		69	5	14	8	8	89		24		35	5.78	0.15
4	A	145	541	16		11	14		7	3	28	14		188				31	6.12	0.13
	B	126	612	15		26	26		31	1	12	5		75		25		45	5.05	0.18
5	A	355	404			3	21			5	7	12	10	72		34		75	5.29	0.16
	B	204	558			9	26			4	6	13	12	62		36		71	5.37	0.17
6	A	461	288			13	15			4	3	32	16	54		22		92	5.49	0.12
	B	275	511			17	21			4	3	19	23	26		25		74	5.16	0.14

Pribyl DW (2010) A critical review of the conventional SOC to SOM conversion factor. Geoderma 156:75–83. doi: 10.1016/j.geoderma.2010.02.003

Figure S1: P *K*-edge bulk-XANES spectra from KMC-1 beamline, HZB (a) and $L_{2,3}$-edge bulk-XANES spectra from VLS-PGM beamline, CLS (b) of P compounds (top) and the A and B horizon soils (bottom); blue arrows show features of Ca-P (apatite), orange arrows of Al associated to P (Al-P) and brown arrows of Fe associated to P (Fe-P).

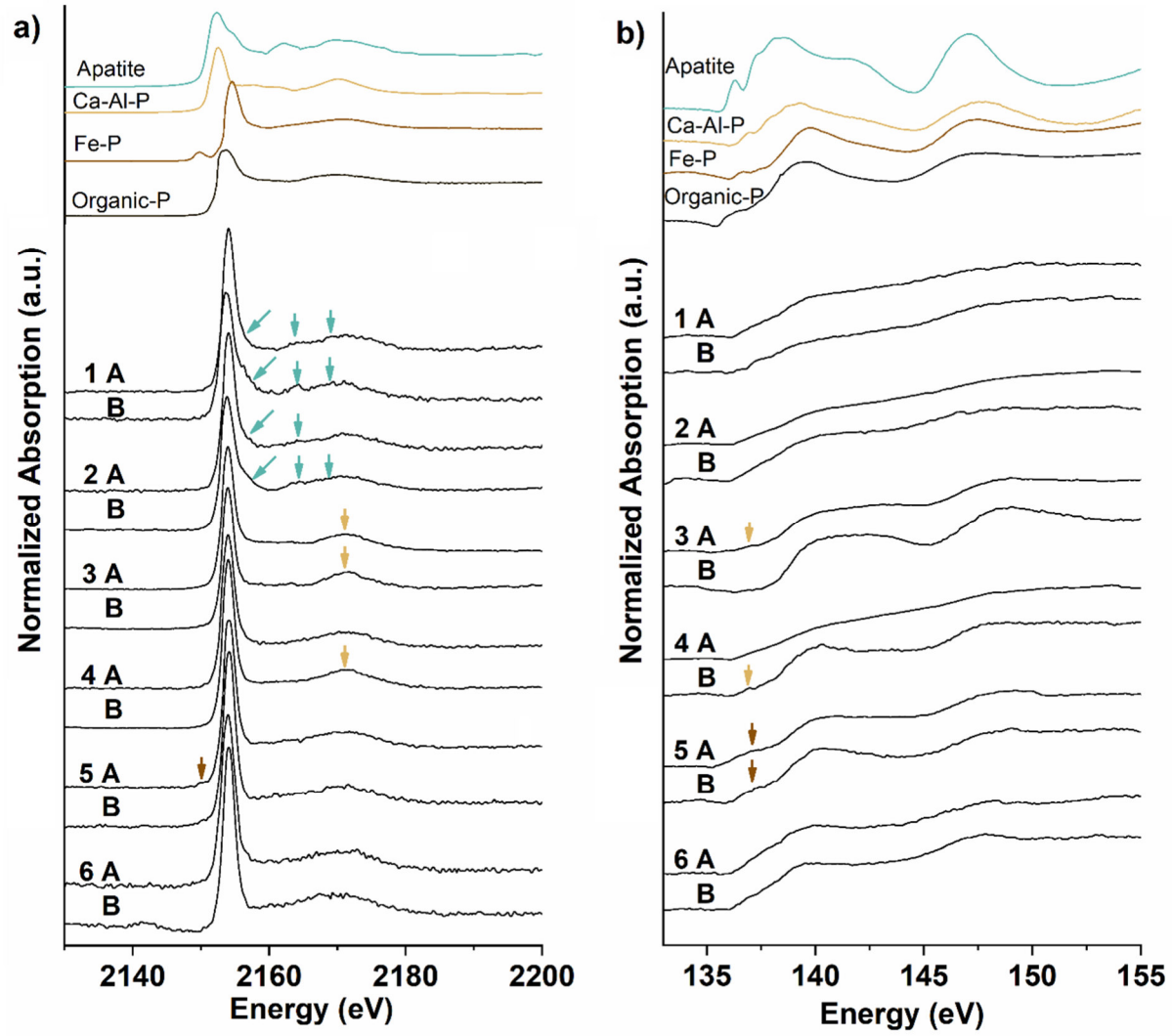

Phosphorus $L_{2,3}$-edge bulk-XANES spectroscopy

P $L_{2,3}$-edge bulk-XANES analysis of the soil samples were carried out at the Variable Line Spacing Plane Grating Monochromator (VLS-PGM) beamline (Hu et al. 2007) at the Canadian Light Source. Because the Hawaiian soils contain more than 3000 mg/kg P they were all analyzable by P $L_{2,3}$-edge XANES spectroscopy (Colocho Hurtarte et al. 2020). The electron storage ring was operated in decay mode with a current range of 220-170 mA. All spectra were recorded at room temperature in the energy range from 130 to 155 eV, with a step size of 0.1 eV and a dwell time of 4 s or 16 s, as a function of the amount of P in the samples. The entrance and exit slits were set to 200 µm. The spectra were collected in total fluorescence yield mode (FLY), using a microchannel plate detector (Kasrai et al. 1993) and were normalized with respect to the incident photon flux (I_0). I_0 was simultaneously recorded with the FLY by monitoring the drain current emitted from a Nickel mesh (90% transmission) located in front of the samples. As for *K*-edge spectra, *L*-edge spectra were analyzed using *Athena* (Ravel and Newville 2005). Furthermore,

phosphorus $L_{2,3}$-edge XANES spectra of various P reference compounds, which were additionally collected are also shown in supplementary Fig. S3.

In general, the P $L_{2,3}$ edge XANES spectra (Fig. S1b) show features in agreement with results of P *K*-edge XANES spectra. Indeed, in comparison to P-references spectra (Fig. S3), the small edge/bump at 137 eV in 3A and 4B may indicate an Al-P. On the other hand, the pre-peak (136-137 eV) in the P $L_{2,3}$-edge XANES spectra of 5A and 5B may indicate P adsorbed to Fe compounds (Xiong et al. 2012).

References:

Colocho Hurtarte LC, Santana Amorim HC, Kruse J, Criginski Cezar J, Klysubun W, Prietzel J (2020) A novel approach for the quantification of different inorganic and organic phosphorus compounds in environmental samples by P L2,3-edge X-ray absorption near-edge structure (XANES) spectroscopy. Environ. Sci. Technol. DOI: 10.1021/acs.est.9b07018

Hu YF, Zuin L, Wright G, Igarashi R, McKibben M, Wilson T, Chen SY, Johnson T., Maxwell D, Yates BW, Sham TK, Reininger R (2007) Commissioning and performance of the variable line spacing plane grating monochromator beamline at the Canadian Light Source. Rev. Sci. Instrum. 78:083109.

Kasrai M, Yin ZF, Bancroft GM, Tan TH (1993) X-ray fluorescence measurements of XANES at the Si, P and S L-edges. J. Vac. Sci. Technol. A 11:2694-2699.

Ravel R, Newville M (2005) ATHENA, ARTEMIS, HEPHAESTUS: data analysis for X-ray absorption spectroscopy using IFEFFIT. J. Synchrotron Radiat. 12:537–541.

Xiong W, Peng J, Hu Y (2012) Use of X-ray adsorption near edge structure (XANES) to identify physisorption and chemisorption of phosphate onto ferrihydrite-modified diatomite. J. Colloid Interface Sci. 368:528-532.

Figure S2. Phosphorus K-edge XANES spectra of various P-references analyzed at KMC-1 beamline, HZB

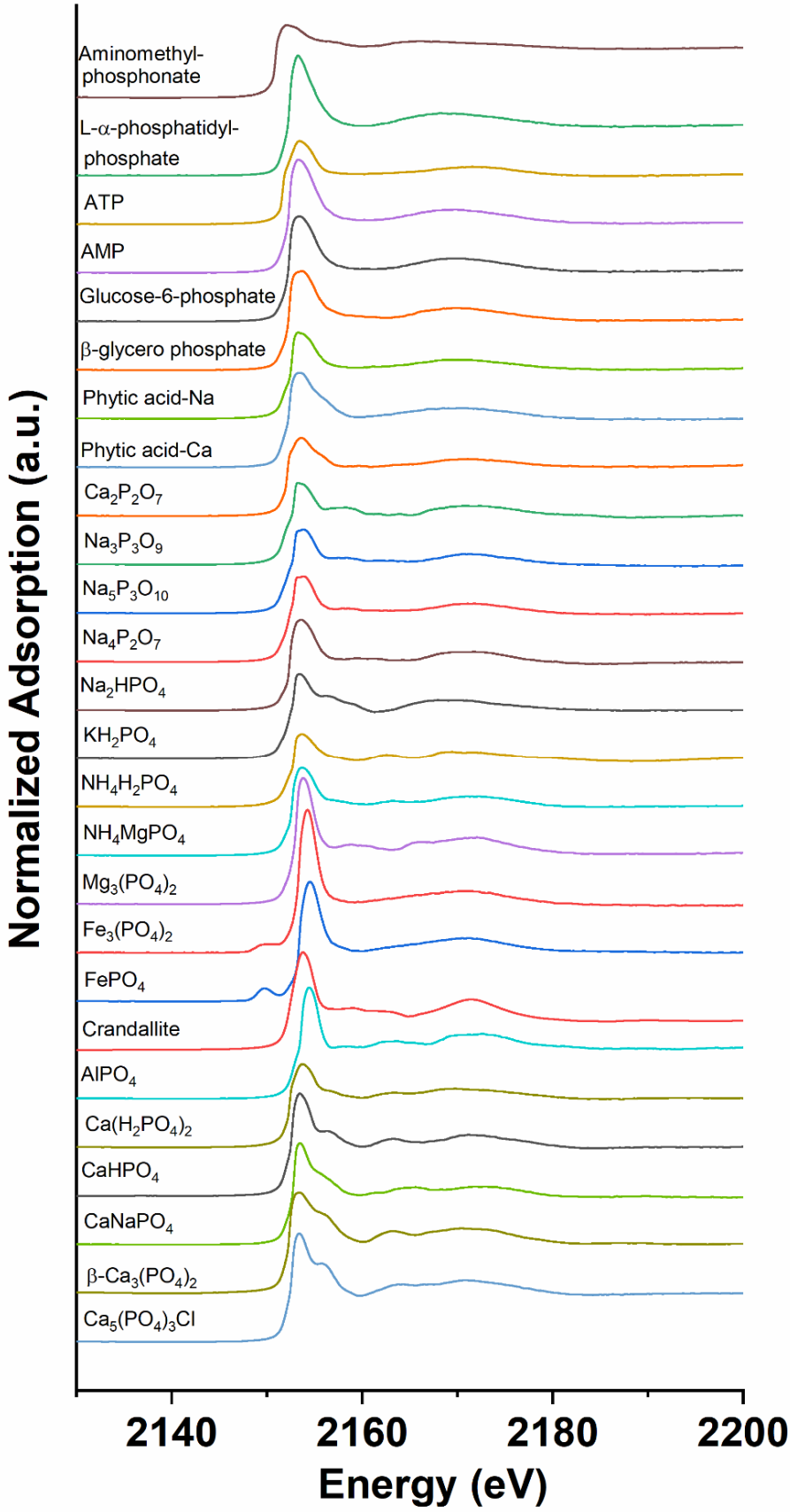

Figure S3: Phosphorus $L_{2,3}$-edge XANES spectra of various P-references analyzed at VLS-PGM beamline, CLS

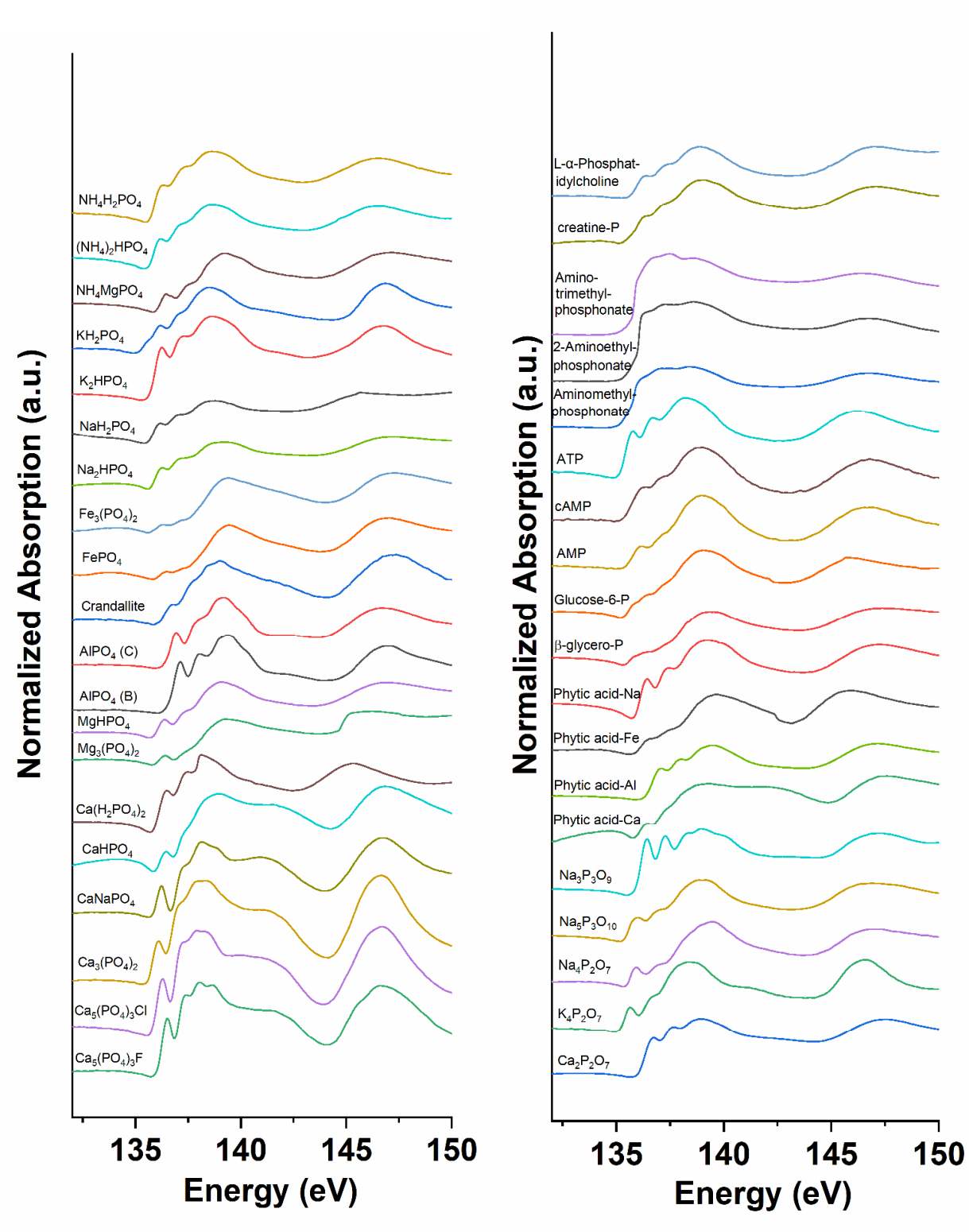

Figure S4: XRF map of P, Ca and Al (left bottom; 0.7 µm step; color scale is arbitrary; white bar is 10 µm), P map with selected points of interest for micro-XANES (left top; red = high concentration, blue = low concentration), and micro-XANES spectra (right, vertical lines show features of same compound) of the soil sample 5A, analyzed at ID21 beamline, ESRF.

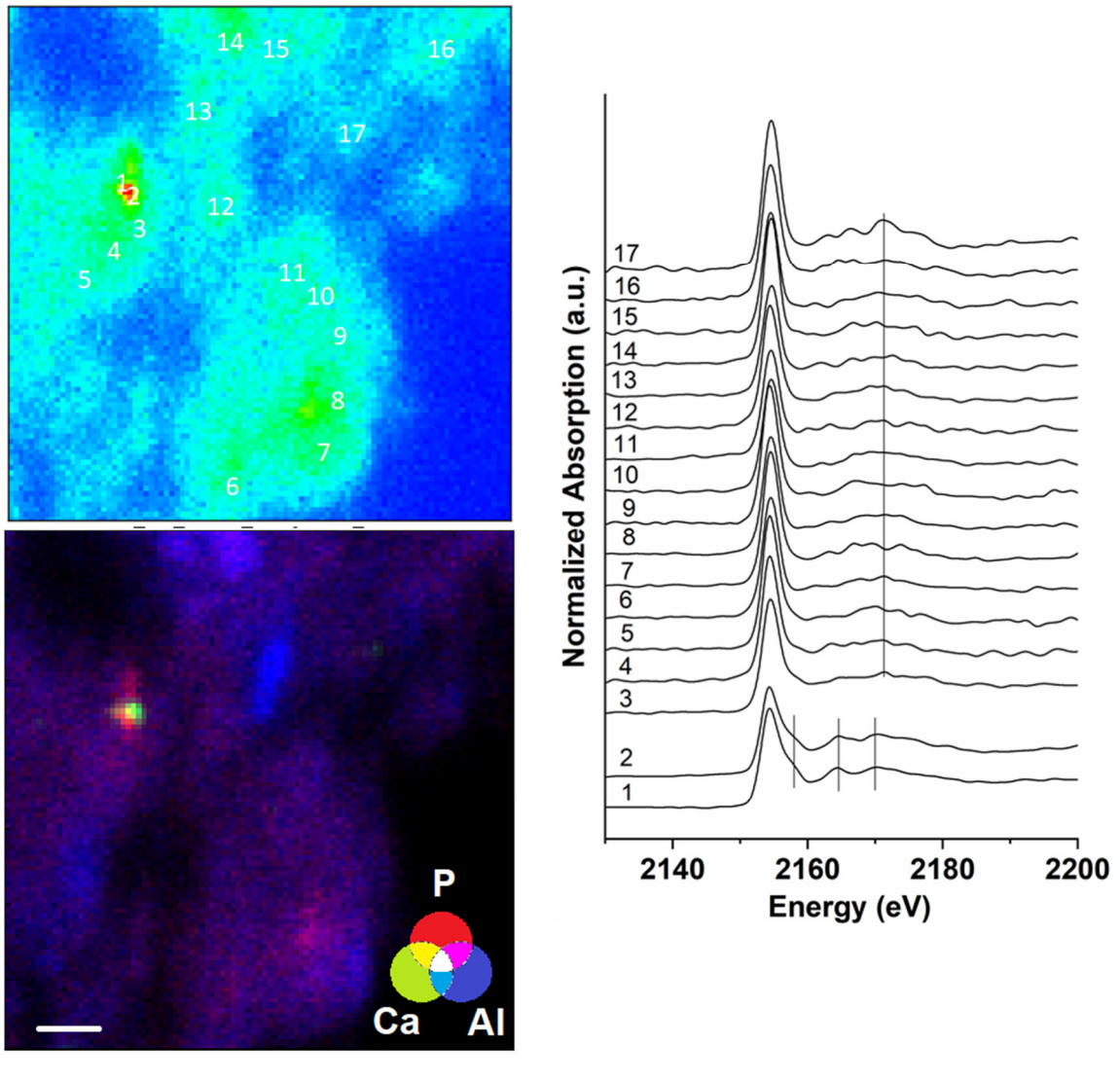

Figure S5: XRF map of P, Fe and Al (left bottom; 5 µm step; color scale is arbitrary; white bar is 25 µm), P map with selected points of interest for micro-XANES (left top; red = high concentration, blue = low concentration), and micro-XANES spectra (right, vertical lines show features of same compound) of the soil sample 6A, analyzed at LUCIA beamline, Soleil

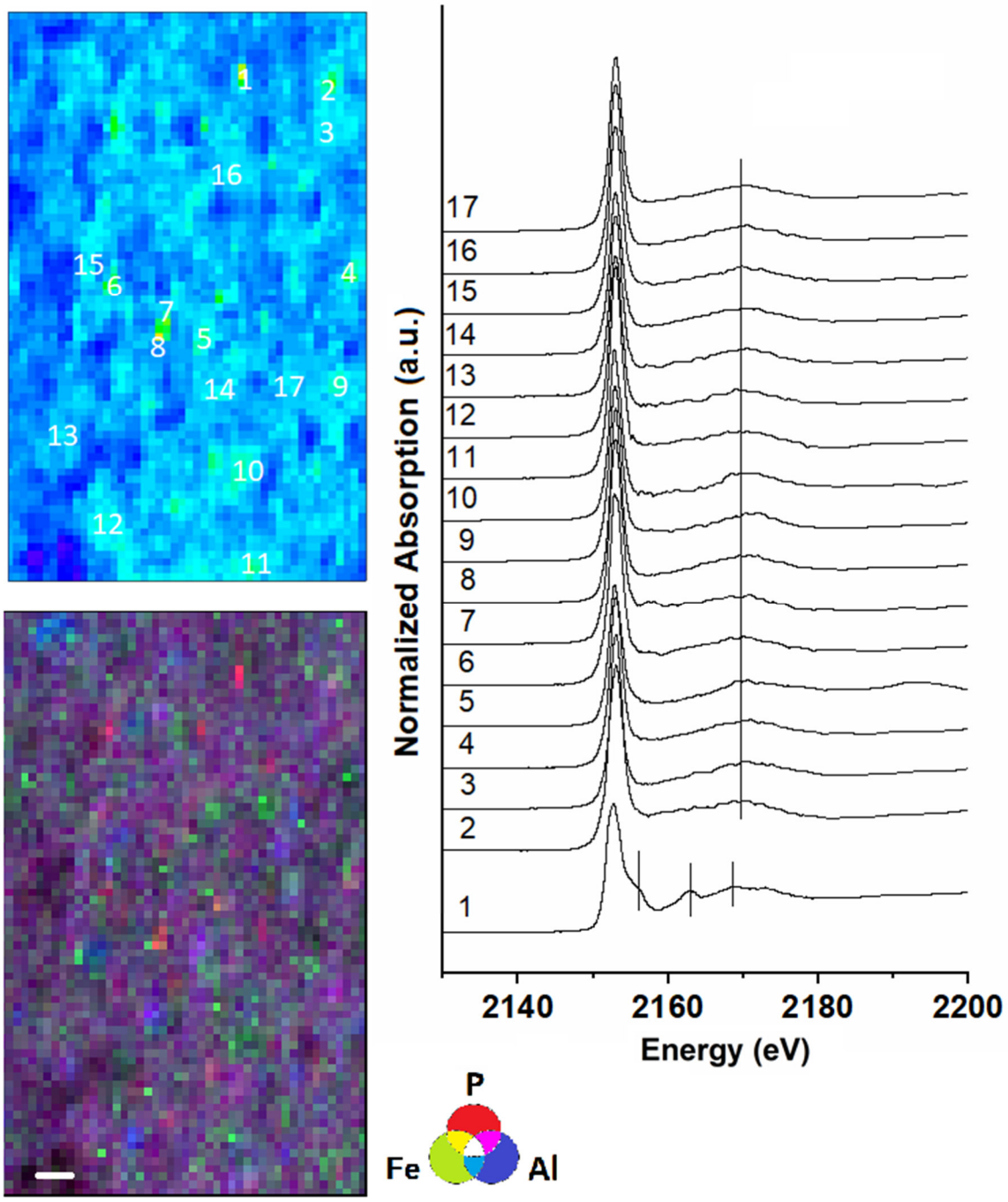

Figure S6: a) XRF P map with selected point of interest for micro-XANES (left; 2 µm step; red = high concentration, blue/violet = low concentration) and b) micro-XANES spectra (right) of the soil sample 6A (green) and apatite reference, analyzed at 14-3 beamline, SSRL.

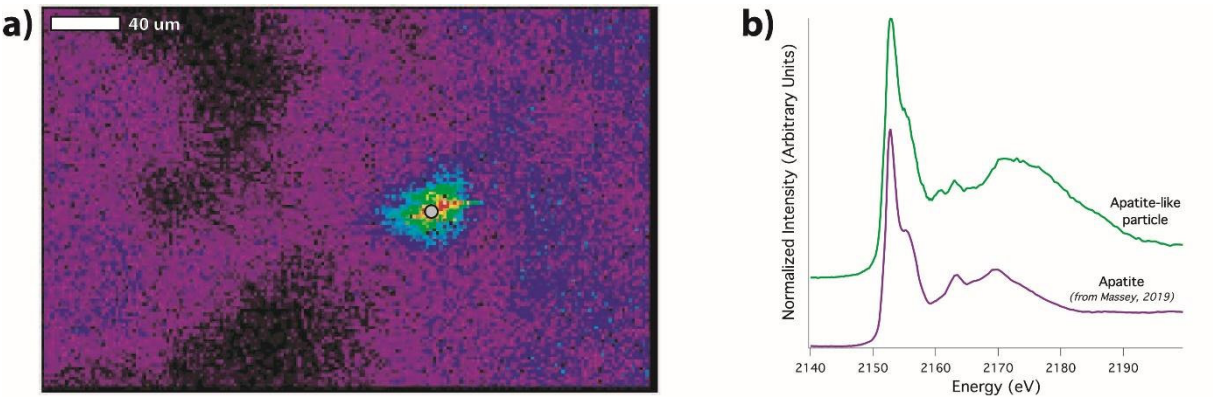

Figure S7: Comparison of Raman spectra from a) reference compounds (green = apatite, orange = anatase, blue = quartz and violet = forsterite) vs. b) Hawaiian soils (microspot spectra from soils 2A and 6A) from RRUFF database